JOURNAL OF MATERIALS SCIENCE 27 (1992) 4772–4781

Microstructure, tensile properties and fracture behaviour of aluminium alloy 7150

T. S. SRIVATSAN
Department of Mechanical Engineering, The University of Akron, Akron, OH 44325, USA

A study has been made to understand the microstructure, tensile properties and fracture characteristics of aluminium alloy 7150. Detailed optical and transmission electron microscopical observations were used to analyse the intrinsic microstructural features of the alloy in the T77 condition. The alloy was deformed to failure over a range of strain rates in environments of 3.5% sodium chloride solution and laboratory air. The environment was found to have little influence on strength of the alloy. The strength only marginally increased with an increase in strain rate. However, for all strain rates, the ductility of the alloy degraded in the aggressive environment. The ratio of strain to failure in sodium chloride solution to that in laboratory air indicates that the alloy is only mildly susceptible to stress corrosion cracking. The fracture behaviour was different in the two environments. However, in a given environment the fracture behaviour was essentially the same. In the aggressive environment fracture was predominantly intergranular while fracture revealed a ductile transgranular failure in laboratory air. An attempt is made to discuss the kinetics of the fracture process in terms of competing mechanistic effects involving intrinsic microstructural features, matrix deformation characteristics, environment and strain rate.

1. Introduction

Over the years, age-hardenable high-strength aluminium alloys belonging to the Al–Zn–Mg family have proved useful as structural materials primarily because they combine unique advantages of low density, high strength and good corrosion resistance. Their usefulness in airframe structures, such as aircraft, space vehicles, and lightweight armoured carriers, has been critical to vehicle performance on account of their superior performance in many aspects, including high strength-to-weight ratio, attractive specific stiffness, low cost, durability, machinability and good formability [1–4]. In recent years, the stringent demands placed by the newer generation aircraft has resurrected considerable scientific and technological interest in the development of new aluminium alloys as attractive alternatives to the existing high-strength commercial alloys. In addition, a progressive increase in fuel prices led to an increased pressure for lighter weight structural components for commercial aircraft, primarily because lighter weight translates to a decrease in both fuel consumption and direct operating costs.

To meet the demands of the aerospace industry, the Aluminum Company of America (ALCOA), in co-operation with Boeing Commercial Airplane Company, developed new aluminium alloys having combinations of improved strength and corrosion resistance combination. For applications requiring high compressive strength, moderate level of fracture toughness and savings in structural weight, the composition limits and heat treatment of aluminium alloy 7050 was modified. The new material was designated by the Aluminum Association as 7150-T6. In this temper, the plates and extrusions of alloy 7150 developed high strength, good fatigue resistance and adequate fracture toughness. Unfortunately, the enhanced strength of this material resulted in a degradation in exfoliation corrosion resistance. In an attempt to improve the resistance to exfoliation corrosion, without sacrificing strength, ALCOA developed a new temper and designated it as T77. Essentially, the T77 temper provided strength levels comparable with 7150-T6 coupled with improved exfoliation corrosion and improved resistance to stress corrosion cracking, in the short transverse direction, with no appreciable loss in strength. This led to the use of alloy 7150, in both plate and extrusion forms, for the upper wing structure of the C-17 military transport aircraft and other specific corrosion sensitive applications [3, 5].

The relationship between microstructure, tensile properties and fracture characteristics of aluminium alloy 7150 is described. The influence of environment and strain rate on tensile properties and fracture behaviour is also highlighted. The kinetics governing the tensile fracture process are discussed in the light of competing mechanistic effects involving intrinsic microstructural features, deformation rate, mode of slip and micromechanisms which promote failure.

2. Material and experimental procedure

The 7150 aluminium alloy used in this study was povided by ALCOA as 25 mm thick plate in the T77

0022–2461

temper condition. The nominal chemical composition (wt %) of the alloy is shown in Table I. The alloy is a modified version of alloy 7050 with lower levels of the elements iron and silicon. Zirconium is added to the alloy to control grain size and/or suppress recrystallization. It combines with aluminium to form the metastable Al_3Zr phase (β') and precipitates during the ingot pre-heat and homogenization treatment. These particles, referred to as dispersoids, play a major role in controlling the fracture process.

Metallographic samples were cut from the three orthogonal directions of the rolled plate, mounted in bakelite and wet ground on 325, 400 and 600 grit silicon carbide (SiC) paper using water as lubricant and then mechanically polished with 1 and 0.05 μm alumina-based lubricants. Grain morphology was revealed using a Keller's etch. The etched specimens were examined in an optical microscope and photographed using a standard bright-field technique.

Cylindrical tensile specimens were machined from the as-received plate. The stress axis of the specimen was parallel to the rolling (longitudinal) direction. The specimens were smooth and cylindrical in the gauge section and conformed to ASTM Standard E8-69. The cylindrical surfaces of all specimens were ground to 600 grit surface finish using silicon carbide paper in order to remove all circumferential scratches and machine marks. Tensile tests were performed on a computer-controlled closed loop servohydraulic test machine in environments of: (a) laboratory air (relative humidity 55% and room temperature of 23 °C), and (b) aerated 3.5% sodium chloride solution. An environmental test chamber, constructed of plexiglass, was used to contain the aqueous sodium chloride solution. To reach stability with the environment the test specimens were exposed to (soaked in) the 3.5% NaCl solution for a predetermined time (40 min) prior to testing.

The effect of deformation rate (strain rate) on monotonic mechanical properties was investigated by testing the alloy at four different strain rates (10^{-5}, 10^{-4}, 10^{-3} and $10^{-2}\,s^{-1}$). The load versus displacement curves were recorded on an $X-Y$ recorder. For the purpose of calculating the reduction in area, the diameter of the tensile samples were measured using a micrometer, before and after testing.

Fracture surfaces of the deformed tensile specimens were examined in a scanning electron microscope (SEM) to determine the predominant fracture mode and to characterize the fine-scale features on the fracture surface. Samples for SEM observation were obtained from the deformed tensile specimens by sectioning normal to the fracture surface.

3. Results and discussion

3.1. Microstructure

The as-received microstructure of the alloy was partially recrystallized with large recrystallized grains that were flattened and elongated in the rolling direction, as a consequence of deformation introduced during rolling (Fig. 1). The grain size was non-uniform along the three orthogonal directions of the wrought plate, resulting in an anisotropic microstructure. At higher magnifications, the insoluble and partially soluble constituent particles were observed to be stratified and distributed along the longitudinal (rolling) direction of the as-received plate. At regular intervals along the longitudinal direction of the as-received plate, clustering of constituent particles was observed (Fig. 2). Transmission electron microscopy observations revealed the microstructure to contain the intermediate η' precipitates dispersed in the matrix (Fig. 3a) and few equilibrium η precipitates in both the matrix and along the grain boundaries (Fig. 3b). The intermediate precipitate η' is reported to be semi-coherent and can be described in terms of a monoclinic unit cell [6], while the equilibrium phase η is coherent with the aluminium matrix and is hexagonal [7]. The cubic Al_3Zr particles were distributed throughout the matrix. There was no evidence of precipitate-free zones at grain boundaries or grain-boundary triple junctions (Fig. 4).

TABLE I Nominal composition of the 7150 alloy (wt %)

Cu	Mg	Zn	Zr	Si	Fe	Ti	Al
2.10	2.36	6.20	0.13	0.07	0.09	0.02	Bal

3.2. Tensile properties

A compilation of monotonic mechanical properties of aluminium alloy 7150, at the four different strain rates, in laboratory air environment, is given in Table II. Multiple samples were tested at each strain rate and no significant variation between the pairs of samples was observed.

The yield strength (0.2% offset) and ultimate tensile strength increased only marginally with an increase in strain rate. The maximum increase in yield strength was 5% and that of the ultimate tensile strength 4%. The total elongation to failure (ductility) decreases with an increase in strain rate from $10^{-5}\,s^{-1}$ to $10^{-2}\,s^{-1}$. No observable trend could be noted for the reduction in area and the true fracture strain ($\ln(A_0/Af)$). The elastic modulus obtained by extensometer trace accords well for the different strain rates.

The results obtained in the aggressive 3.5% sodium chloride solution are summarized in Table III. Here again, it is observed that both yield strength and ultimate tensile strength increase only marginally with deformation rate or strain rate. The maximum increase in yield strength was 4.4% and of ultimate tensile strength 5.0%. The total elongation to failure degrades with strain rate, and the total elongation at a given strain rate is observed to be 50% of the corresponding value in laboratory air. The reduction in area and the true fracture strain ($\ln(A_0/A_f)$) decrease with an increase in strain rate from $10^{-5}\,s^{-1}$ to $10^{-2}\,s^{-1}$.

Several explanations and models exist for strength and ductility variations with strain rate [8, 9]. It is recognized that face centred cubic metals like aluminium are insensitive to strain rate. The results summarized in Tables II and III conform to this observation, but for only a marginal increase (4%–5%)

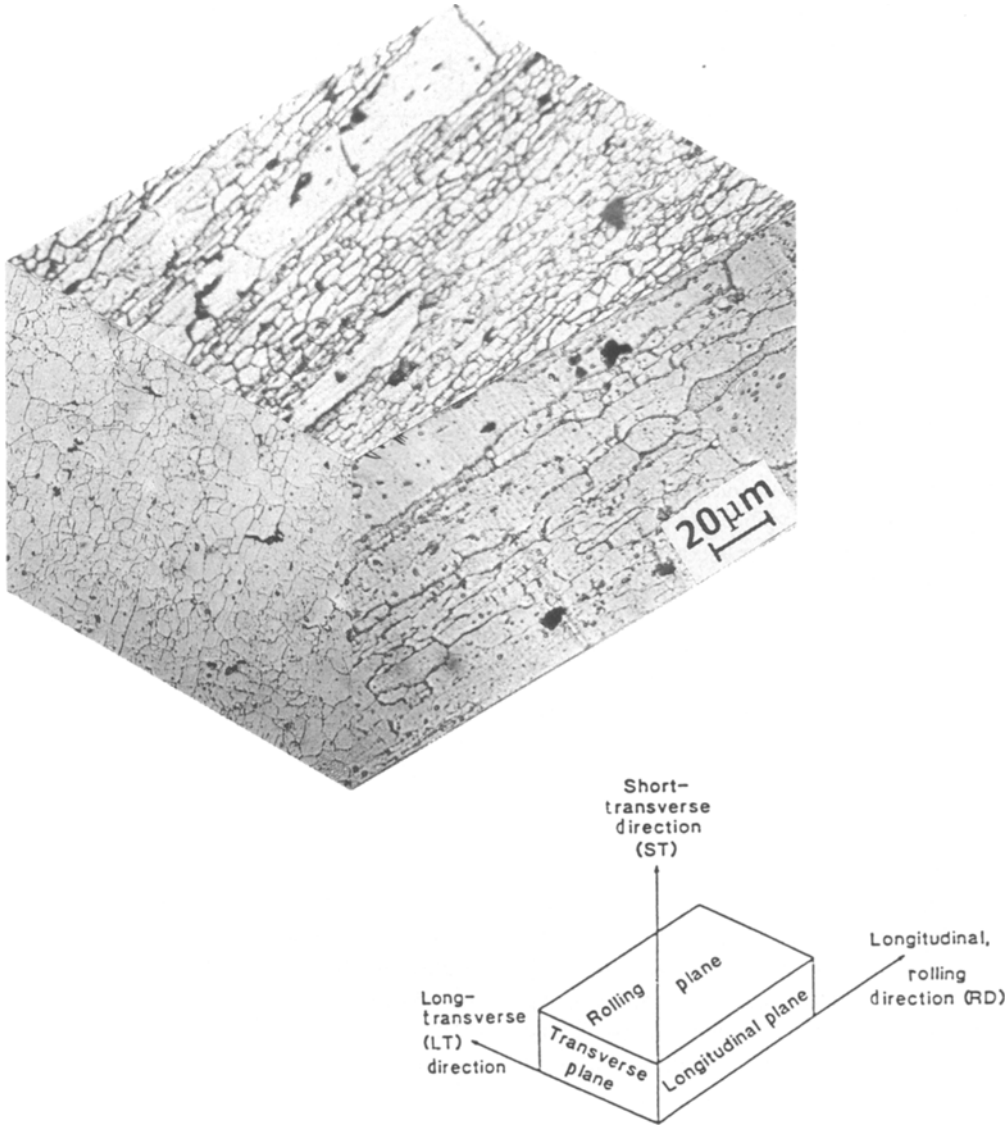

Figure 1 Triplanar optical micrograph illustrating the grain structure of alloy 7150-T77.

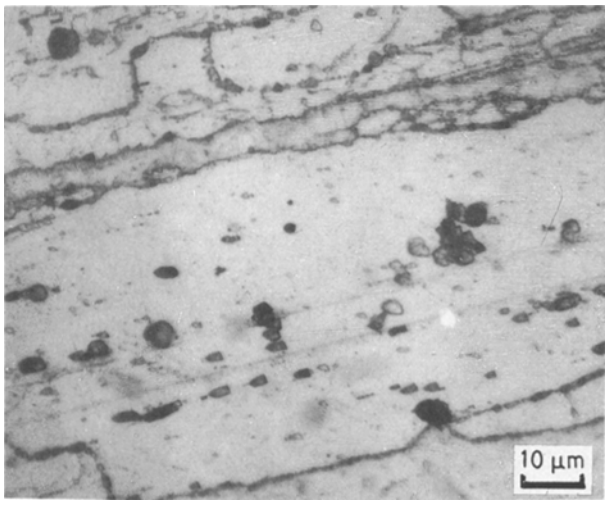

Figure 2 Optical micrograph showing clustering of intermetallic particles in the rolling direction of the plate.

in both yield strength and ultimate tensile strength with an increase in strain rate. A comparison of the tensile strength and total strain to failure in the two environments is provided in Table IV. It is established that an increase in tensile strength is accompanied by a decrease in tensile ductility (elongation to failure) in both laboratory air and 3.5% sodium chloride solution.

The influence of test environment on tensile properties can be rationalized on the basis of several competing effects, the most important of which is total test time. At a strain rate of $10^{-5}s^{-1}$ the time of exposure of the test specimen to the environment is several times more than at the higher strain rates. A slower strain rate provides for increased test time which allows for greater interaction of the material with the environment. Consequently, effects of the aggressive environment on mechanical properties of aluminium alloy 7150 is felt at the lower strain rate than at the higher strain rates. The ratio of strain (total) to failure when tested in the 3.5% sodium chloride solution to that in laboratory air (Table IV) provides a measure of susceptibility of the alloy to stress corrosion cracking (SCC). The effect of strain rate on the ratio is small and the ratio decreases marginally with decreasing strain rate, indicating a susceptibility of the alloy to stress corrosion cracking at lower strain or deformation rates.

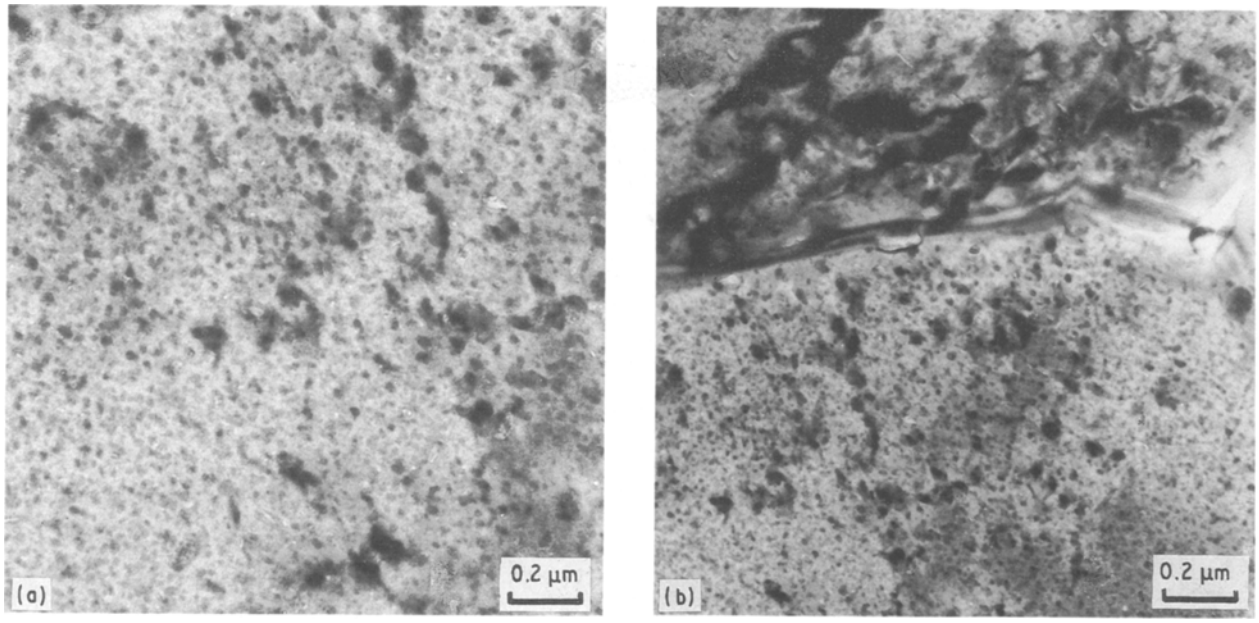

Figure 3 Bright-field transmission electron micrograph of aluminium alloy 7150-T77 showing (a) intermediate precipitates in the matrix (b) equilibrium precipitate in the matrix and at the grain boundary.

TABLE II Monotonic mechanical properties[a] of aluminium alloy 7150-T77 (environment: laboratory air)

Strain rate (s^{-1})	Yield strength		Ultimate tensile strength		Total elongation to failure (%)	Reduction in area (%)	True strain $\varepsilon_f^* = \ln(A_0/A_f)$ (%)
	(MPa)	(10^3 p.s.i)	MPa	(10^3 p.s.i)			
0.000 01	524	(76)	552	(80)	70	21	24
0.000 1	545	(79)	559	(81)	65	23	26
0.001	552	(80)	568	(82)	60	23	26
0.01	548	(79.5)	572	(83)	57	17	19

[a] Results are mean based on two tests.

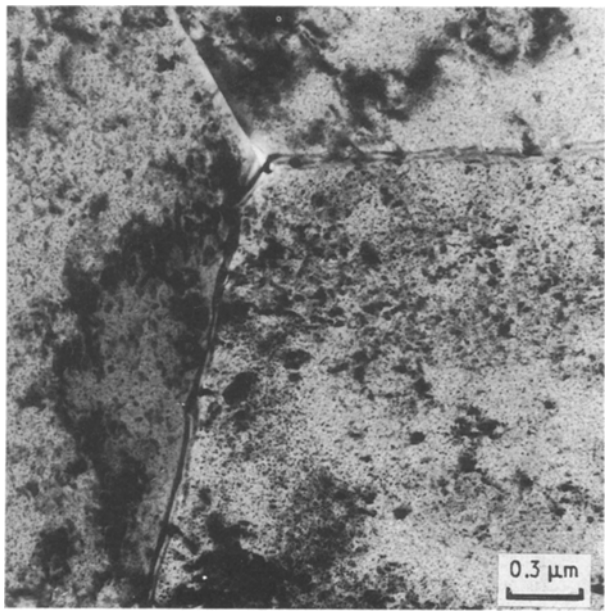

Figure 4 Bright-field transmission electron micrograph showing the absence of a precipitate-free zone at the grain boundary.

The susceptibility of the alloy to SCC at very low strain rates is interpreted as being due to the competing influence of two independent mechanisms: (1) film rupture–anodic dissolution, and (2) hydrogen-induced cracking. For the film rupture–anodic dissolution mechanism, the strain-induced rupture of the passive film at the crack tip is followed by crack initiation. Formation and rupture of the protective film is dependent on strain rate. In the hydrogen-induced cracking mechanism the hydrogen generated, in the moist environment, from a local reaction can penetrate short distances into the lattice and eventually to the grain boundaries, provided the oxide film is not a barrier. The depth of hydrogen penetration is controlled by matrix deformation characteristics. The hydrogen accumulates at the grain-boundary precipitates, such as η particles, and promotes intergranular rupture when the local fugacity becomes high [10–12]. The extent and depth of hydrogen penetration and accumulation at grain-boundary regions is also dependent on the time of exposure to the environment or strain rate.

Although the strain-rate dependence of ratio of total strain at failure in aqueous sodium chloride to that in laboratory air (relative humidity 55%) indicates a very small or limited susceptibility of the alloy to stress corrosion cracking at lower strain rates, the specific mechanism, film rupture–anodic dissolution or hydrogen-induced cracking, is difficult to discern.

TABLE III Monotonic mechanical properties[a] of aluminium alloy 7150 (environment: 3.5% NaCl solution)

Strain rate (s^{-1})	Yield strength		Ultimate tensile strength		Total elongation to failure (%)	Reduction in area (%)	True strain $\varepsilon_f^* \ln(A_0/A_f)$ (%)
	(MPa)	(10^3 p.s.i)	MPa	(10^3 p.s.i)			
0.000 01	517	(75)	559	(81)	34	23	26
0.000 1	524	(76)	566	(82)	35	23	26
0.001	538	(78)	579	(84)	32	22.5	25
0.01	540	(78)	586	(85)	30	19	21

[a] Results are mean based on two tests.

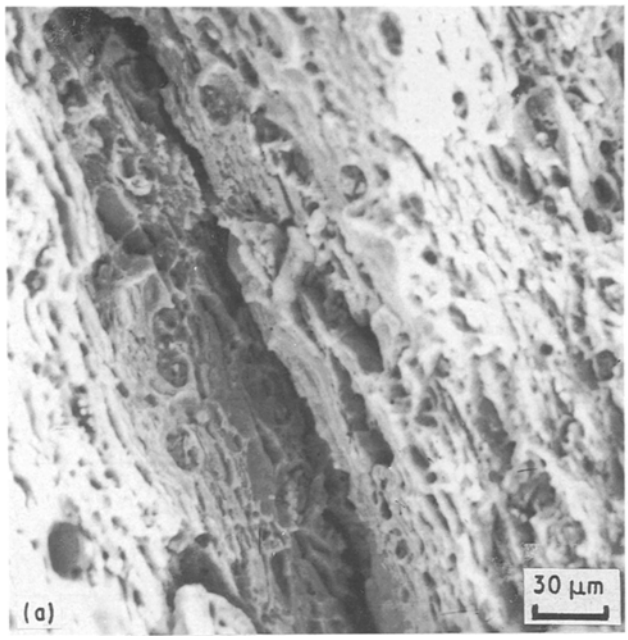

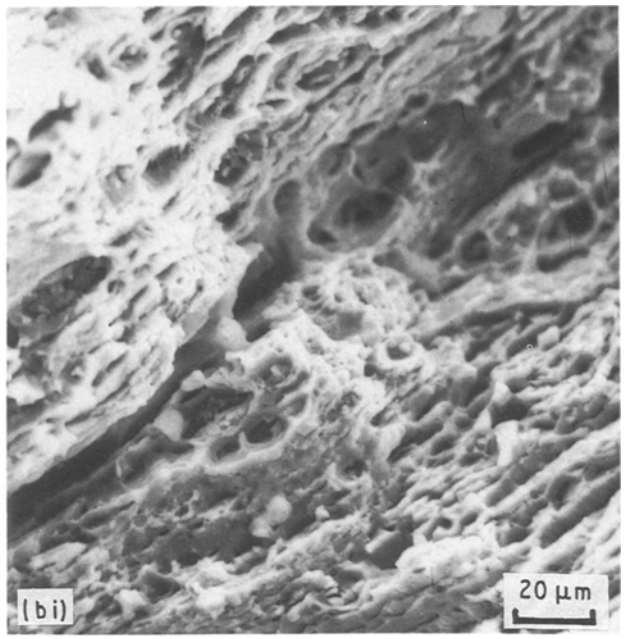

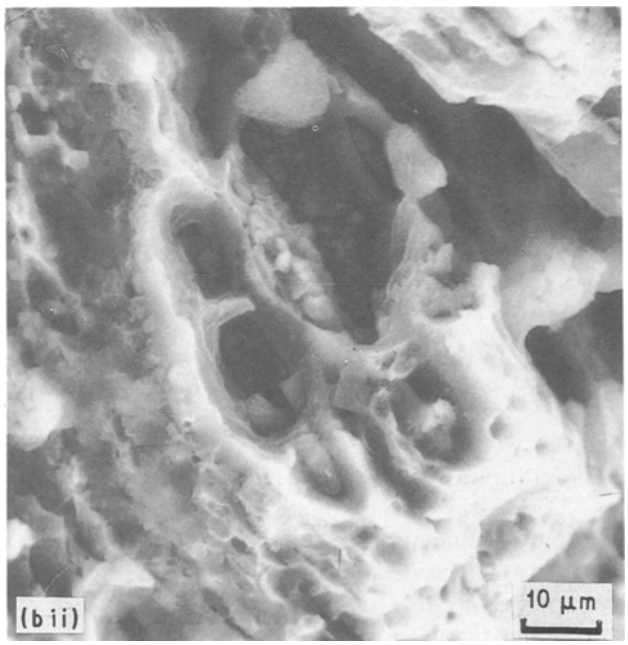

Figure 5 Scanning electron micrographs of a sample deformed at 0.000 01 s^{-1} in 3.5% NaCl solution, showing (a) intergranular cracking, and (b) bimodal distribution of voids.

3.3. Deformation and fracture characteristics

The monotonic fracture surfaces are helpful in elucidating microstructural effects on ductility and fracture properties of alloy 7150. Examination of the fracture surface features in a scanning electron microscope (SEM) of the deformed tensile specimens were done at low magnification to identify the overall fracture morphology, and at higher magnification to identify the fine-scale fracture surface features. Fractography of the tensile samples revealed different features in the two environments. Representative fracture features of the deformed tensile samples are shown (Figs 5–8) for both environments.

Extensive fractography of the tensile samples revealed on a macroscopic scale the tensile fracture of alloy 7150-T77 deformed at the lower strain rate [0.01 $\times 10^{-3}$ s^{-1}] to be predominantly shear in both environments. The fracture surfaces were oriented approximately 30° to the major stress axis. Fracture of the deformed tensile samples in the aggressive sodium chloride environment revealed an overall macroscopically brittle appearance at low magnifications, and a microscopically ductile appearance, with evidence of voids and shallow dimples on fracture surface, at higher magnifications. On a macroscopic scale, fracture was found to be bimodal with cracking evident

TABLE IV Comparison of properties of aluminium alloy 7150-T77 in laboratory air and 3.5% sodium chloride solution

Strain rate (s^{-1})	Sodium chloride		Laboratory air		$(\varepsilon_f)_{NaCl}$
	ε_f (%)	UTS (MPa)	ε_f (%)	UTS (MPa)	$(\varepsilon_f)_{Lab\ air}$
0.000 01	34	559	70	552	0.48
0.000 1	35	566	65	559	0.53
0.001	32	579	60	568	0.53
0.01	30	586	57	572	0.52

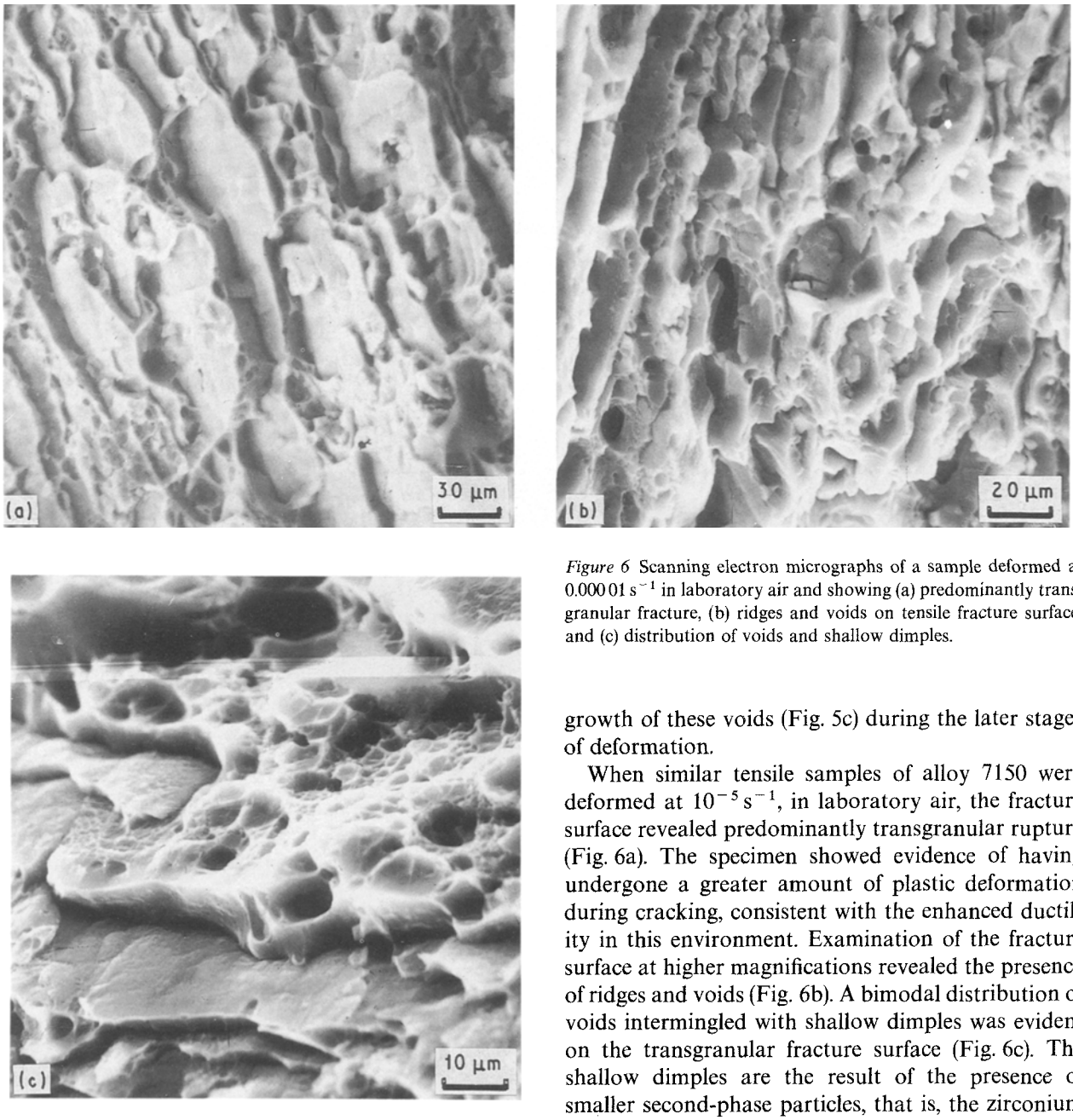

Figure 6 Scanning electron micrographs of a sample deformed at 0.000 01 s^{-1} in laboratory air and showing (a) predominantly transgranular fracture, (b) ridges and voids on tensile fracture surface, and (c) distribution of voids and shallow dimples.

along the high-angle grain boundaries (Fig. 5a). Examination of the fracture surface at high magnification revealed an existence of a population of voids of a wide range of sizes distributed uniformly throughout the fracture surface. The macroscopic voids were intermingled with microscopic voids indicating ductile rupture (Fig. 5b). The applied stress assists in the growth of these voids (Fig. 5c) during the later stages of deformation.

When similar tensile samples of alloy 7150 were deformed at $10^{-5}\,s^{-1}$, in laboratory air, the fracture surface revealed predominantly transgranular rupture (Fig. 6a). The specimen showed evidence of having undergone a greater amount of plastic deformation during cracking, consistent with the enhanced ductility in this environment. Examination of the fracture surface at higher magnifications revealed the presence of ridges and voids (Fig. 6b). A bimodal distribution of voids intermingled with shallow dimples was evident on the transgranular fracture surface (Fig. 6c). The shallow dimples are the result of the presence of smaller second-phase particles, that is, the zirconium dispersoids $\beta'(Al_3Zr)$ and the equilibrium η precipitates. In laboratory air, strain rate was found to have little influence on overall fracture behaviour. That is, failure was observed to be ductile in appearance both at the macroscopic and microscopic level. Typical fracture features in the aggressive NaCl solution at strain rates of 10^{-5} and $10^{-3}\,s^{-1}$ are shown in Fig. 7. The fracture consisted predominantly of intercrystalline cracking. The cracks were observed along grain boundaries (Fig. 7b), and extending in the direction of

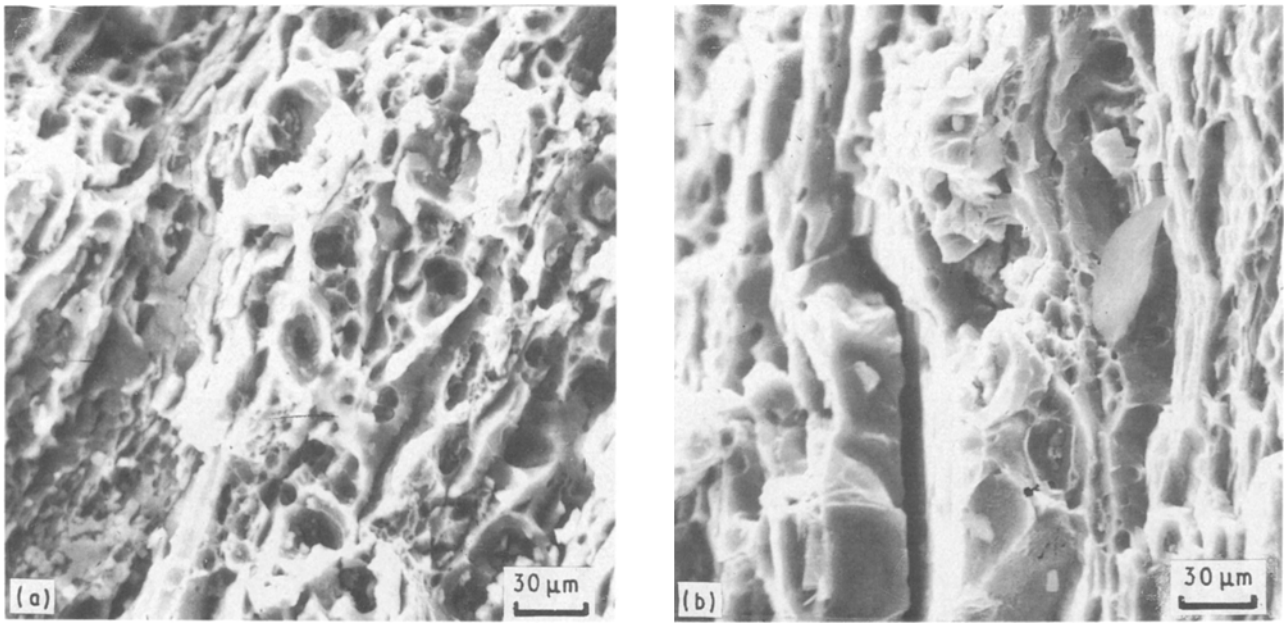

Figure 7 Comparison of tensile fracture features of test samples deformed in 3.5% sodium chloride solution at strain rates of (a) 0.001 s^{-1}, (b) 0.000 01 s^{-1}.

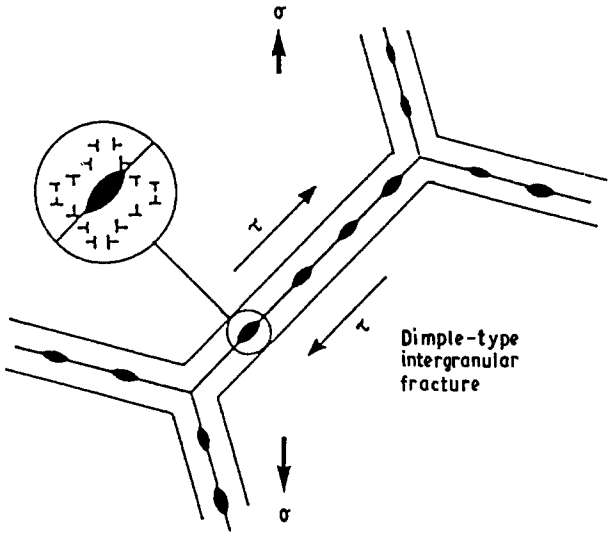

Figure 8 Schematic representation of the dimple-formation type intergranular fracture.

the tensile axis, suggesting the importance of normal stress during deformation. Some regions displayed macroscopic voids. Because crack extension under quasi-static loading occurs at high stress intensities, comparable with the fracture toughness of the material, the presence of macrovoids and microvoids lowers the strain to failure associated with ductile failure.

The intermetallics in this alloy are the iron-rich particles, the silicon-rich particles, and small quantities of large undissolved magnesium-rich phases. During plastic deformation, nucleation of cracks and void initiation occurs (i) by cracking of the coarse constituent particles, such as Al_7Cu_2Fe [13], (ii) by decohesion along the particle/matrix interface [14, 15], and (iii) at areas of poor inter-particle bonding [16, 17, 18]. Interfacial strength is a dominant factor in crack initiation. There are several other factors which, though secondary and indirect compared to particle/matrix separation, contribute to the void-initiation process. These include (a) the size of the second-phase particle, (b) particle shape and volume fraction, (c) particle strength, (d) particle location, and (e) distribution of particles in the matrix [15]. Void initiation at the coarse-constituent particle is a complex combination of inclusion size, local stress and strain levels, and local deformation modes. The presence of fairly large second-phase particles in the matrix facilitates the nucleation of cracks at low to moderate stress levels [18]. Void nucleation at a coarse second-phase particle occurs when the elastic energy in the particle exceeds the surface energy of the newly formed void surfaces [18]. For the case of spherical particles, the critical stress for particle cracking is

$$\sigma = (6\gamma E/q^2 d)^{0.5} \quad (1)$$

where γ is the surface energy of the particle, q is the stress concentration factor at the particle, E is the Young's modulus of the particle, and d is the particle diameter.

While satisfying the above equation is a necessary condition for void nucleation, it must also be aided by a stress on the particle/matrix interface in excess of the interfacial strength [20]. When the stress at the particle/matrix interface reaches a critical value, void nucleation occurs by separation at the interface. The interface stress, σ_1, at a particle comprises of the applied stress, σ_A, and the normal stress due to localized deformation, that is, blocked slip bands, σ_P

$$\sigma_1 = \sigma_A + (\sigma_P) \quad (2)$$

When a critical value of the interface stress is reached, void nucleation occurs provided sufficient elastic energy is available to create new void surfaces. Furthermore, in alloy 7150 containing coarse second-phase particles, there exists an intrinsic particle-size effect on void nucleation [19]. The influence of particle size is caused by the interaction of their stress fields. Argon

and co-workers [19, 20] suggested that when large particles are closely spaced their stress/strain fields interact, giving rise to higher local stress/strain than otherwise anticipated, thus enabling critical stress/strain for void nucleation to be attained at lower applied stress. The mutual interaction of particle stress field is initially insignificant but increases or builds up once necking occurs resulting in a large number of particles nucleating voids.

Coalescence of microvoids is the distinct phase or the last stage in the ductile fracture process. During coalescence, void–void interactions occur during which period void growth is accelerated. In 7150 alloy, void coalescence results from synergistic interaction of (a) the formation of void sheets at the smaller second-phase particles, that is, the $\beta'[Al_3Zr]$ dispersoids, and (b) void impingement, that is, voids growing until they touch. The large voids which are created by fracture of the coarse iron-rich intermetallic particles coalesce by impingement. The more widely separated voids coalesce by the formation of void sheets. Coalescence of microvoids initiated at grain-boundary precipitates results in dimple-formation type intergranular fracture (Fig. 8).

The micromechanisms governing the deformation and resultant fracture characteristics of an age-hardenable aluminium alloy depend on the intrinsic microstructural features, such as (i) coherency and distribution of matrix precipitates, (ii) grain size and shape, (iii) grain-boundary precipitates, and (iv) the presence of other second-phase particles including the dispersoids and insoluble constituent particles which result from the iron and silicon impurities. The concentration of deformation in planar bands (Fig. 9) leads to strain localization at their point of impingement on the grain boundary. The localized deformation produces a large stress concentration at the grain boundary. This effect coupled with the presence of grain-boundary precipitates results in enhanced deformation along the grain boundaries. Void initiation results at the intersection of a slip band and a coarse grain-boundary precipitate (Fig. 10). The applied stress assists in the growth of voids. The fine microvoids coalesce and the halves of these voids are the dimples visible on the fracture surface (Fig. 11). Shallow dimples were found covering the intergranular fracture regions (Fig. 12) indicative of limited ductile behaviour.

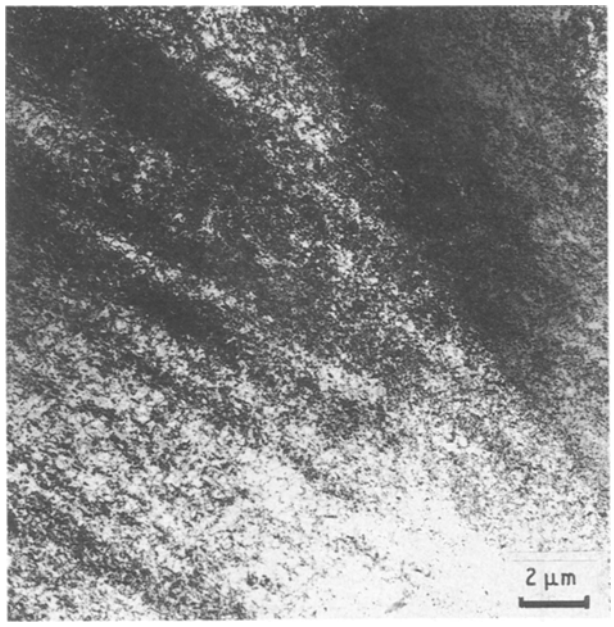

Figure 9 Bright-field transmission electron micrograph showing planar deformation bands in alloy 7150-T77 deformed in tension in laboratory air at $0.000\,01\ s^{-1}$.

4. Conclusions

Based on a study of microstructure, tensile properties and fracture characteristics of aluminium alloy 7150-

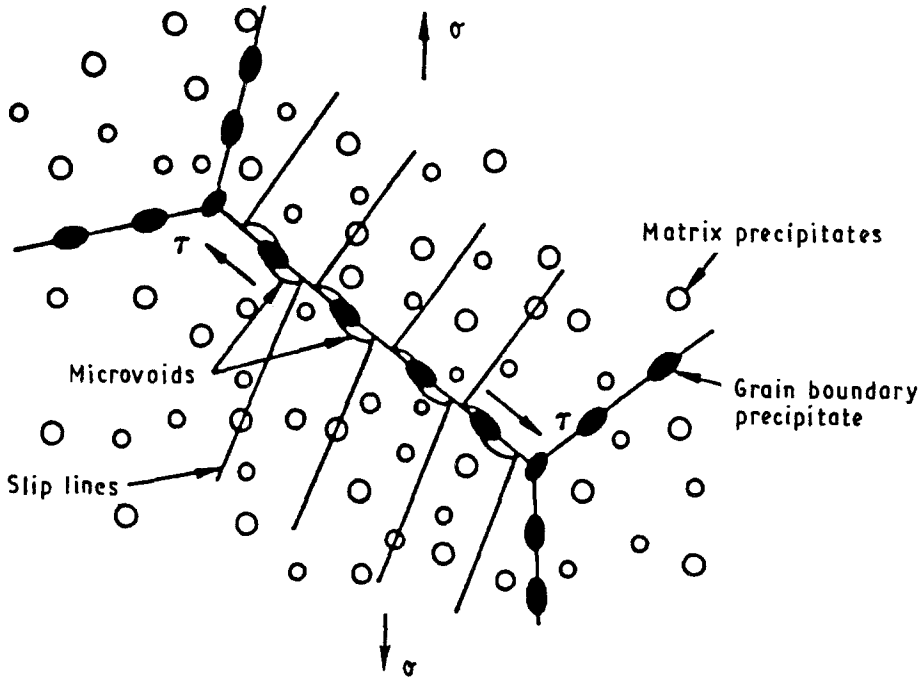

Figure 10 Schematic representation of the deformation process in the absence of a precipitate-free zone and with grain-boundary particles.

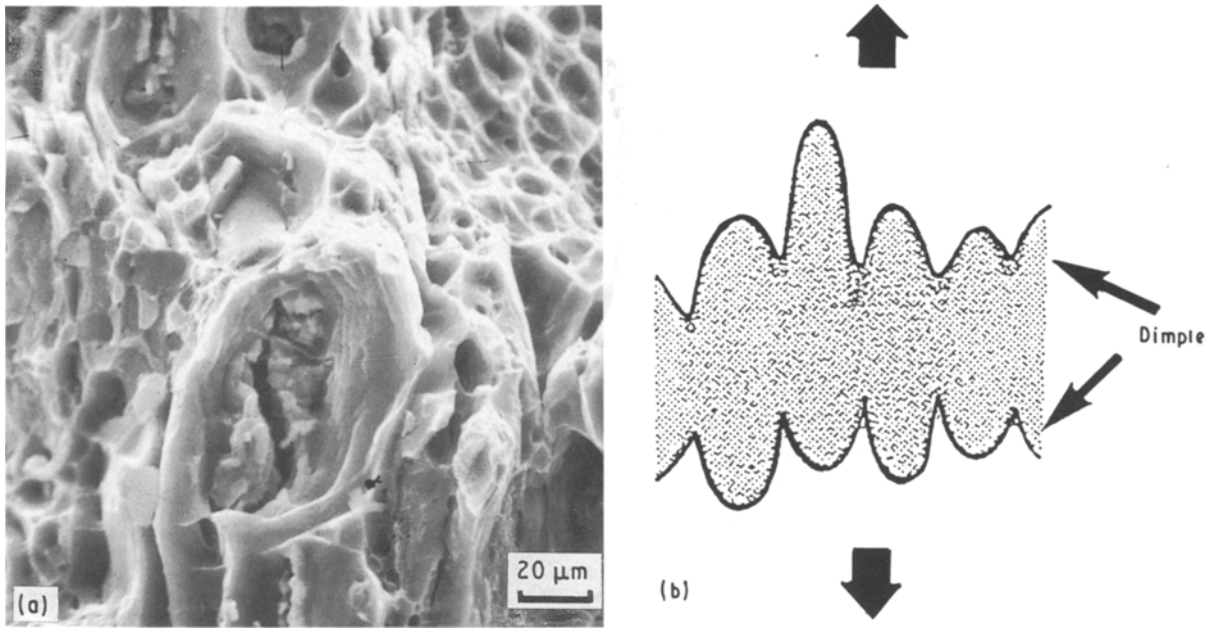

Figure 11 (a) Scanning electron micrograph showing dimples and microvoids on a transgranular fracture surface. (b) Schematic representation of a dimple on a transgranular fracture surface.

Figure 12 Scanning electron micrograph showing shallow dimples on the intergranular fracture surface.

T77 tested over a range of strain rates in environments of laboratory air and 3.5% sodium chloride solution, the following conclusions were drawn.

1. The alloy is partially recrystallized with the grains elongated parallel to the rolling direction. At regular intervals clustering of the coarse constituents was found.

2. Environment was found to have little influence on yield strength and ultimate tensile strength of the high-purity alloy. However, strength increased only marginally with an increase in strain rate.

3. Ductility, expressed through total elongation to failure, decreased with an increase in strain rate in both test environments. The aggressive sodium chloride solution caused a degradation in ductility of the alloy. The degradation was as high as 50%.

4. The ratio of total strain to failure in the two environments offers a measure of susceptibility to stress corrosion cracking and reveals the alloy to have very limited susceptibility.

5. At all strain rates fracture in the aggressive environment revealed an overall macroscopically brittle but a microscopically ductile appearance with evidence of voids and dimples. In the less aggressive laboratory air, fracture surfaces of the tensile deformed samples was predominantly transgranular with macroscopic and microscopic voids intermingled with shallow dimples on the transgranular fracture surface.

Acknowledgements

The present work was supported by the University of Akron under Faculty Research Grant no. 2-07064. Alloy used in this study was provided by the Aluminium Company of America. Thanks and appreciation are extended to Dr Warren H. Hunt, Jr. and A. K. Vasudevan for their help in procuring the material. The authors thank Mr Joe Lucas, Akron Machining Institute, for his timely assistance in providing test samples used in this study.

References

1. J. T. STALEY, "Microstructure and Toughness of High Strength Aluminum Alloys", ASTM STP 304 (American Society for Testing Materials, Philadelphia, PA, 1976).
2. J. T. STALEY, in "Encyclopedia of Physical Science and Technology, 1989 Yearbook", edited by R. A. Meyers (Academic Press, New york, 1989) pp. 177–83.
3. E. A. STARKE Jr, *Mater. Sci. Engng* **29** (1977) pp. 99–112.
4. J. T. STALEY, in "Aluminum Alloys: Contemporary Research and Applications", edited by R. Doherty and A. K. Vasudevan (Academic Press, New York, 1989) pp. 3–31.
5. P. R. BRIDENBAUGH, *Aluminium, Int. J.* **65** (1989) No. 7/8, pp. 771–782.

6. J. GJONNES and C. J. SIMENSEN, *Acta Metall.* **18** (1970) 881.
7. L. F. MONDOLFO, *Metals Mater.* **5** (1971) 95.
8. F. A. McCLINTOCK and A. S. ARGON, "Mechanical Behavior of Materials" (Addison Wesley, Reading, MA, 1966) pp. 190–5.
9. L. E. MALVERN, in "Mechanical Properties at High Rates of Strain", edited by J. Harding (The Institute of Physics, London, UK, 1984) pp. 1–20.
10. W. GRUHL, *Z. Metallkd* **75** (1984) 819.
11. T. D. BURLEIGH, *Corrosion* **47** (1991) 89.
12. N. J. HOLROYD, A. K. VASUDEVAN and L. CHRISTODOULOU, in "Aluminum Alloys", edited by A. K. Vasudevan and R. D. Doherty (Academic Press, New York, 1989) pp. 463–83.
13. J. GURLAND and J. PLATEAU, *Trans. ASM* **56** (1963) 442.
14. R. H. VAN STONE and J. A. PSIODA, *Metall. Trans.* **6A** (1975) 672.
15. R. H. VAN STONE, J. R. LOW and J. L. SHANNON, *ibid.* **9A** (1978) 539.
16. R. H. VAN STONE, T. B. COX, J. R. LOW Jr and J. A. PSIODA, *Int. Met. Rev.* **30** (1985) 157.
17. T. S. SRIVATSAN and E. J. COYNE Jr *Mater. Sci. Technol.* **3** (1987) 130.
18. A. W. THOMPSON, *Metall. Trans.* **18A** (1987) 1877.
19. A. S. ARGON, *J. Eng. Mater. Technol.* **98** (1976) 60.
20. A. S. ARGON, J. IM and A. NEEDLEMAN, *Metall. Trans.* **6A** (1975) 825.

Received 7 May
and accepted 12 September 1991